

■ Loss of immiscible nitrogen from metallic melt explains Earth's missing nitrogen

J. Liu, S.M. Dorfman, M. Lv, J. Li, F. Zhu, Y. Kono

■ Supplementary Information

The Supplementary Information includes:

- 1. Synchrotron X-ray Radiography Experiments
- 2. Chemical Analysis of Recovered Samples
- 3. The Evolution of the BSE C/N Ratio during Core Formation
- Table S-1
- Figures S-1 to S-10
- Video S-1
- Supplementary Information References

1. Synchrotron X-ray Radiography Experiments

High-pressure and high-temperature synchrotron X-ray radiography experiments were conducted at the beamline 16-BM-B of the Advanced Photon Source (APS), Argonne National Laboratory (ANL). High-pressure conditions were generated by using a VX-3 Paris-Edinburgh (PE) press with a pair of cup-shaped tungsten carbide anvils having 12 mm-diameter cup and 3 mm-diameter bottom (Kono *et al.*, 2015). High resolution images were recorded by using a CCD camera (Prosilica GC1380H) about 30 cm away from the sample position (Kono *et al.*, 2015). The full field of view for this camera is 1.3 mm (horizontal) by 1.0 mm (vertical) and the frame rate is 1 frame/second while the Video S-1 displays at 3 times faster speed.

A standard PE sample assembly configuration was employed (Kono *et al.*, 2014), where X-ray transparent MgO sample capsules were used to prevent nitrogen contamination instead of commonly-used BN capsule. The initial size of the cylindrical sample charge was 1.5 mm in diameter and 2.0 mm in height. The starting materials Fe₃N (99.9 %) and Fe₄N (99.9 %) were commercially available (Kojundo Chemical Lab. Co. Ltd.), and Fe-N mixtures with 1.4 wt. %, 3.0 wt. % N were prepared by mixing fine-grained Fe₃N powder and Fe power (99.998 %, Alfa Aesar). For Fe-N-C starting materials, fine-grained graphite powder (99.9 %) is added to the required level. All the starting materials were dried at 373 K in a vacuum oven overnight. For each experiment, the sample was first compressed to a target pressure and heated gradually to a target temperature through graphite heater outside the MgO capsule. Pressures were determined *in-situ* by the thermal equation of state of MgO sample capsule, and temperatures were estimated by established power-temperature curves (Kono *et al.*, 2014). *In situ* energy-dispersive X-ray diffraction (EDXD) measurements at $2\theta = 15^\circ$ with a beam size of 0.1*0.3 mm² were conducted to confirm the crystal structures of the solid phases and monitor the evolution of melting (Fig. S-1). Temperatures were quenched by shutting off the power supply under high pressures to preserve the liquid compositions for chemical analysis.



2. Chemical Analysis of Recovered Samples

The chemical compositions of recovered samples were analysed using the Cameca SX-100 electron microprobe in University of Michigan. Electron beam conditions were 15 kV and 20 nA for Fe; 11 kV and 70 nA for C; 11 kV and 150 nA for N. The detection limit was ~ 500 ppm for all of the three elements. A Ni/C multilayer crystal (PC2) was used for analysing nitrogen and carbon, while a LiF crystal was used for Fe measurements (LLIF). Samples were Al coated together with standards in order to keep the conductive layer uniform. Si₃N₄ (99.9 %, Alfa Aesar) was used as nitrogen standard while pure iron and Fe₃C were used as Fe and C standards, respectively. The accuracies of C and N measurements were checked by measuring Fe₃N and Fe₃C standards, which yielded compositions Fe₃N_{0.97(2)} and Fe₃C_{0.95(2)}, respectively. The fast diffusivities of Fe, C and very likely also N in metallic liquid (~10⁻⁷ m² s⁻¹, Dobson and Wiedenbeck, 2002) would ensure equilibrium being reached. The chemically homogenous and time-independent compositions of run products (Table S-1) are evidence that chemical equilibrium was reached in our high-pressure melting experiments. For experiments using Fe-N starting materials, electron microprobe analysis indicates that the quenched samples also have 0-1.6 wt. % C (Table S-1). C contamination likely originated from the graphite heater outside MgO capsule.

3. The Evolution of the BSE C/N Ratio during Core Formation

We develop a three-step model for calculating N and C evolution during accretion and core formation. In the first step, the alloy and silicate components of impactors are in equilibrium and the mass ratio of alloy and silicate parts is set at 0.46, the same as the Earth's core/mantle mass ratio. In the second step, impacts induce extensive melting and N stored in the alloy is assumed to be released as immiscible fluid. The amount of N subject to loss to space during impacts depends only on initial N content of the alloy, which is set by the oxygen fugacity of the impactors, with higher N stored in alloy in oxidised impactors (Fig. S-9). In the third step, C and the residual N are re-distributed among atmosphere, silicate mantle and metallic core on the basis of mass balance. In this step, we consider re-equilibration of alloy droplets with the magma ocean to be inefficient: a fraction of alloy droplets exchange C and N with atmosphere and silicate to match equilibrium partitioning, while the remaining alloy droplets keep their original C/N ratio.

In our model, the initial equilibrium distribution of N and C in the alloy and silicate phases of impactors are calculated based on the following equations:

$$M_{i,\text{metal}} = D_{i,\text{metal/silicate}} \cdot f \cdot M_i / (1 + D_{i,\text{metal/silicate}} \cdot f) \quad \text{Eq. S-1}$$

$$M_{i,\text{silicate}} = M_i / (1 + D_{i,\text{metal/silicate}} \cdot f) \quad \text{Eq. S-2}$$

Here M_i is the total mass of N or C carried by impactors. $M_{i,\text{metal}}$ and $M_{i,\text{silicate}}$ are the mass of N or C stored in metallic and silicate phases of the impactors, respectively. f is the metal-silicate mass ratio: $f = \text{mass}_{\text{core}} / \text{mass}_{\text{mantle}}$, which is set to 0.46 as the averaged value to resemble the Earth's core/mantle mass ratio. $D_{i,\text{metal/silicate}}$ is N or C partition coefficient between metallic and silicate phases. The relations between $M_{i,\text{metal}}$ and f at different oxygen fugacity are shown in Figure S-9.

In the second step, we assume that all N stored in impactors' metallic phase is lost during collision with magma ocean to immiscible N-dominant liquid, and then to the space. In the third step (core formation), the fate of C and residual N is described by the model proposed in Bergin *et al.* (2015); Dalou *et al.* (2017); Hirschmann (2016). In this model, the mantle is in equilibrium with overlying atmosphere. Nitrogen-depleted metallic melt delivered by impacts descends through the magma ocean, and the degree of re-equilibration between metallic and silicate melts is an input parameter. Because of the significant difference in C/N ratios between alloy and silicate of impactors, we only consider the part of alloy droplets in equilibrium with magma ocean in the mass conservation (Eq. S-3). The remaining alloy from impactors would transport all its C to the core.

The total mass of C ($M_{\text{C}}^{\text{Total}}$) involved in mass conservation during core formation is as follows:

$$M_{\text{C}}^{\text{Total}} = M_{\text{C}_0}^{\text{silicate}} + f_1/f \cdot M_{\text{C}_0}^{\text{alloy}} \quad \text{Eq. S-3}$$

Here $M_{\text{C}_0}^{\text{silicate}}$ and $M_{\text{C}_0}^{\text{alloy}}$ are the mass of C stored in silicate and alloy of impactors, respectively. f_1 is the degree of re-equilibration between descending alloy droplets and magma ocean ($f_1 = m^{\text{alloy}} / m^{\text{silicate}}$, m^{alloy} and m^{silicate} are the mass of the involved alloy and silicate portions, respectively. m^{silicate} is assumed to be the same as the current mantle, 4×10^{27} g).

Because N originally stored in alloy is assumed to be lost, the total mass of N ($M_{\text{N}}^{\text{Total}}$) equals to that stored in silicate part of impactors.

$$M_{\text{N}}^{\text{Total}} = M_{\text{N}_0}^{\text{silicate}} \quad \text{Eq. S-4}$$

Based on Bergin *et al.* (2015), $(M_{\text{C}_0}^{\text{silicate}} + M_{\text{C}_0}^{\text{alloy}}) / (M_{\text{N}_0}^{\text{silicate}} + M_{\text{N}_0}^{\text{alloy}}) = 25$.



During core formation, M_C^{Total} and M_N^{Total} redistribute among atmosphere, mantle and core, as described in Bergin *et al.* (2015); Dalou *et al.* (2017); Hirschmann (2016):

$$M_i^{\text{Total}} = M_i^{\text{atmosphere}} + M_i^{\text{silicate}} + M_i^{\text{alloy}} \quad \text{Eq. S-5}$$

where $M_i^{\text{atmosphere}}$, M_i^{silicate} , M_i^{alloy} are volatile mass in atmosphere, silicate and involved alloy, respectively.

The concentrations (C_i) of C and N in silicate and metallic melts are controlled by the partition coefficient ($D_i^{\text{alloy/silicate}}$) and the degree of re-equilibration between alloy and silicate melts. Their relations are listed below:

$$C_i^{\text{silicate}} = M_i^{\text{silicate}} / m^{\text{silicate}} \quad \text{Eq. S-6}$$

$$C_i^{\text{alloy}} = M_i^{\text{alloy}} / m^{\text{alloy}} \quad \text{Eq. S-7}$$

$$D_i^{\text{alloy/silicate}} = C_i^{\text{alloy}} / C_i^{\text{silicate}} \quad \text{Eq. S-8}$$

Volatile concentration in silicate melt is determined by its vapour partial pressure (P_i) and its solubility (S_i) into silicate melt:

$$C_i^{\text{silicate}} = S_i \cdot P_i \quad \text{Eq. S-9}$$

where P_i is calculated by the force generated by this volatile in atmosphere divided by the Earth's surface area (A , $5.1 \times 10^{14} \text{ m}^2$):

$$P_i = r \cdot M_i^{\text{atmosphere}} \cdot g / Z \quad \text{Eq. S-10}$$

where g is the gravitational acceleration; r is the mass ratio between the volatile species and the element of interest. For example, r for CO_2 equals to 44/12 and r for graphite is 1.

Combining Equations S-5 to S-10, volatile mass in atmosphere can be expressed as the following equation:

$$M_i^{\text{atmosphere}} = M_i^{\text{Total}} / [(S_i \cdot r \cdot g / A) \cdot (m^{\text{silicate}} + D_i^{\text{alloy/silicate}} \cdot m^{\text{alloy}}) + 1] \quad \text{Eq. S-11}$$

$$M_i^{\text{silicate}} = [M_i^{\text{Total}} \cdot (S_i \cdot r \cdot g / A) \cdot m^{\text{silicate}}] / [(S_i \cdot r \cdot g / A) \cdot (m^{\text{silicate}} + D_i^{\text{alloy/silicate}} \cdot m^{\text{alloy}}) + 1] \quad \text{Eq. S-12}$$

$$M_N^{\text{alloy}} = [M_N^{\text{Total}} \cdot (S_N \cdot r \cdot g / A) \cdot D_N^{\text{alloy/silicate}} \cdot m^{\text{alloy}}] / [(S_N \cdot r \cdot g / A) \cdot (m^{\text{silicate}} + D_N^{\text{alloy/silicate}} \cdot m^{\text{alloy}}) + 1] \quad \text{Eq. S-13}$$

$$M_C^{\text{alloy}} = [M_C^{\text{Total}} \cdot (S_N \cdot r \cdot g / A) \cdot D_C^{\text{alloy/silicate}} \cdot m^{\text{alloy}}] / [(S_N \cdot r \cdot g / A) \cdot (m^{\text{silicate}} + D_C^{\text{alloy/silicate}} \cdot m^{\text{alloy}}) + 1] + (1 - f_i / f) \cdot M_{C0}^{\text{alloy}} \quad \text{Eq. S-14}$$

M_C^{alloy} is the sum of C in alloy droplets involved in partitioning and the part directly merges with the core without interaction with magma ocean. Under different oxygen fugacity, the distribution of C and N in each reservoir is plotted in Figure S-10. The relations between BSE C/N ratios and f_i at different redox conditions are shown in Figure 3. Notably, the calculated BSE C/N are based on available C and N partitioning data up to ~7 GPa (*e.g.*, Grewal *et al.*, 2019), therefore partitioning study at higher P - T conditions is needed to better quantify the pressure effect on the calculated BSE C/N ratios.



Supplementary Tables

Table S-1 A summary of compositions of quenched samples from high-pressure and high-temperature Paris-Edinburgh experiments. All results were determined by electron microprobe. The first column is N-content of the starting Fe/Fe-N materials. Columns three to six describe the compositions of quenched run products. Carbon contamination may originate from the graphite heater outside the MgO capsule.

Starting N ¹ (wt. %)	Starting C ² (wt. %)	Run product (wt. %)				Run #	Max P ⁴ GPa	Max T ⁵ K	Status before quenching
		Fe	N	C	Total				
0	0	100.1(4)	BDL ³	0.7(4)	100.8(5)	6-17	7.2	2100	1 liquid
1.4	0	98.9(6)	BDL	1.6(1)	100.5(6)	5-17	0.01	2216	2 liquids
1.4	0	99.5(3)	0.6(1)	0.5(1)	100.7(4)	8-17	0.1	1824	2 liquids
1.4	0	97.7(4)	1.4(3)	BDL	99.1(5)	2-16	1.4	2000	1 liquid
3.0	0	100.1(2)	BDL	0.4(2)	100.5(3)	1-17	0.01	2010	2 liquids
3.0	0	98.2(2)	0.6(1)	1.1(4)	99.9(5)	2-17	1.1	2167	2 liquids
3.0	0	98.4(3)	1.1(1)	BDL	99.5(3)	3-17	2.1	1984	2 liquids
5.9	0	97.6(9)	1.5(1)	BDL	99.1(9)	4-16	0.9	1963	2 liquids
5.9	0	98.4(3)	1.5(1)	BDL	100.0(4)	7-17	1.8	1815	2 liquids
5.9	0	95.4(9)	3.1(1)	1.1(1)	99.7(9)	5-16	2.6	1990	2 liquids
7.7	0	98.9(5)	0.6(1)	0.5(2)	100.0(5)	9-17	0.1	1781	2 liquids
7.7	0	98.1(5)	1.5(1)	0.3(1)	99.9(5)	4-17	0.4	1808	2 liquids
7.7	0	92.8(2)	6.1(2)	BDL	98.9(3)	13-18	4.6	2273	2 liquids
7.7	0	92.8(2)	6.8(2)	0.2(1)	99.8(3)	14-18	6.3	2273	2 liquids
5.0	5.0	95.2(1)	BDL	4.5(2)	99.7(2)	8-18	0.9	1503	2 liquids
5.0	5.0	94.6(4)	BDL	5.3(5)	99.9(3)	1-18	1.2	1825	2 liquids
5.0	5.0	92.9(2)	1.8(4)	4.9(3)	99.6(5)	9-18	3.1	2223	2 liquids
5.0	5.0	91.6(2)	3.2(2)	4.9(2)	99.7(3)	11-18	6.6	2273	2 liquids
1.0	5.0	94.7(6)	BDL	4.9(6)	99.6(8)	7-18	0.2	1443	2 liquids
1.0	5.0	93.8(3)	0.5(3)	4.8(5)	99.0(7)	10-18	2.4	2213	2 liquids
1.0	10.0	95.0(8)	BDL	4.8(5)	99.8(9)	5-18	0.3	2248	Gr ⁶ + 2 liquids
1.0	10.0	95.6(2)	BDL	4.7(2)	100.3(3)	12-18	0.5	1478	Gr+ 2 liquids

¹: Uncertainty is ~ 0.3 wt. %; ²: Uncertainty is ~0.4 wt. %; ³: Below detection limit. Detection limit for both N and C is ~500 ppm; ⁴: Pressure is calculated based on thermal equation of state of MgO capsule with an uncertainty of ~0.2 GPa (Kono *et al.*, 2010); ⁵: Temperature is estimated based on power curve with an uncertainty of about 40 K (Kono *et al.*, 2014); ⁶: graphite.



Supplementary Figures

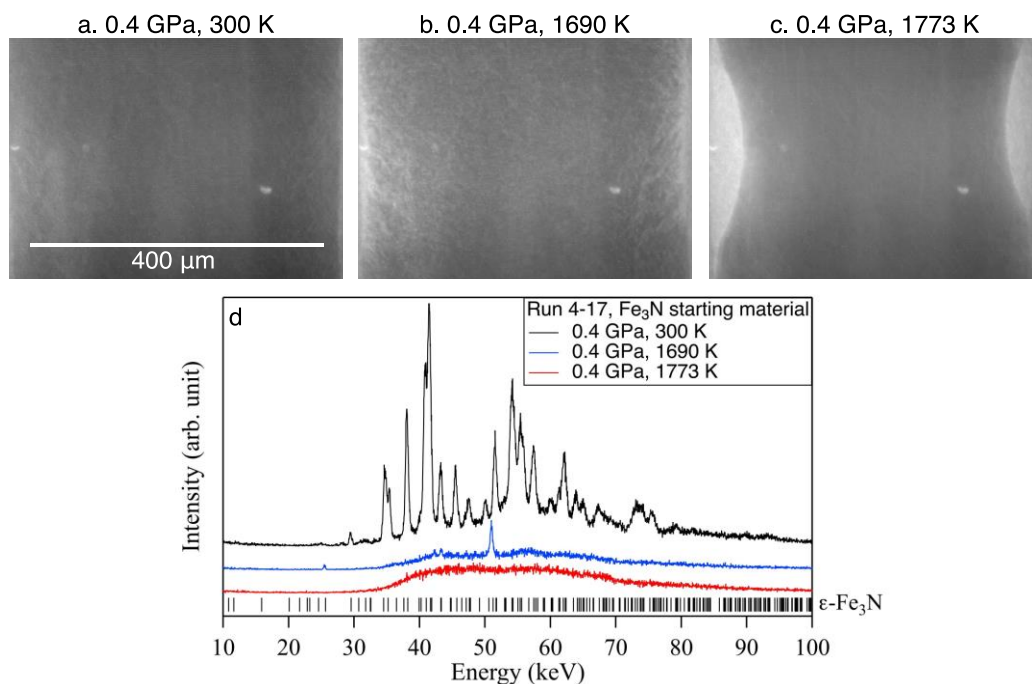


Figure S-1 X-ray radiographic images and the corresponding energy-dispersive X-ray diffraction patterns showing the melting process of Fe_3N at ~ 0.4 GPa and 1773 K (run 4-17). **(a-c)** X-ray radiographic images monitor the evolution of the sample chamber with increasing temperature. **(d)** The ambient temperature XRD pattern matches well with the expected peak positions of $\epsilon\text{-Fe}_3\text{N}$ with the space group P312 (black ticks); at 1690 K (b), only two XRD peaks are present with significant diffuse scattering signal. This indicates a partially molten state; at 1773 K, no XRD peaks appear so the Fe-N sample was fully molten.

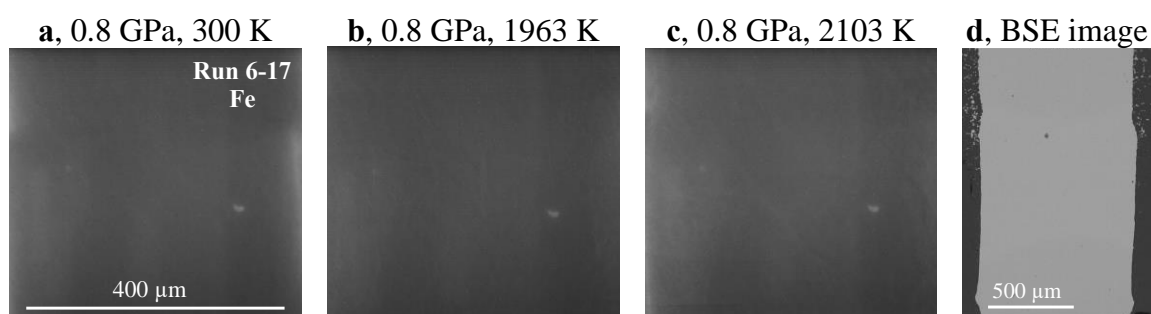


Figure S-2 No immiscible liquids are observed in Fe melting experiment. Run 6-17 with Fe as the starting material is compressed to 0.8 GPa first **(a)** and heated gradually up to 2103 K **(b-c)**. During the heating cycle, no obvious change is shown in *in-situ* X-ray radiographic images. **(d)** BSE image of recovered sample from 7.2 GPa and 2100 K with 0.7 wt. % C, probably from graphite heater.

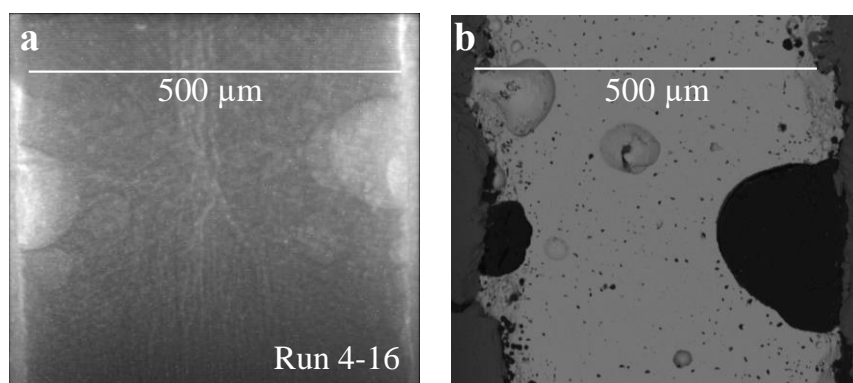


Figure S-3 X-ray radiographic and back-scattered-electron (BSE) images of quenched sample from 0.9 GPa and 1963 K with Fe_4N as the starting composition (run 4-16). The light droplets in X-ray radiographic image (a) correspond to the voids shown in the BSE image (b). The recovered sample contains 1.5 wt. % nitrogen, lower than the starting Fe_4N (5.9 wt. % nitrogen), supporting the conclusion that the light droplets are composed of nitrogen-rich supercritical fluid.

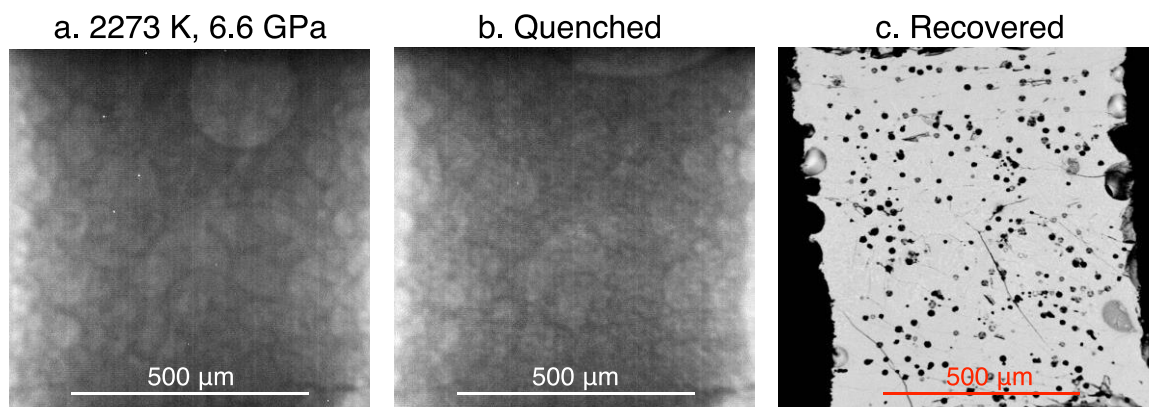


Figure S-4 X-ray radiographic and back-scattered-electron (BSE) images of the experiment run 11-18 quenched from 6.6 GPa and 2273 K with Fe-5.0 wt.% N-5.0 wt. % C as the starting composition. (a, b) *In-situ* X-ray radiographic images of the sample chamber at 6.6 GPa, 2273 K and after quenching in temperature. (c) BSE image of the recovered sample. The black round regions are void and correspond to the locations of N-rich supercritical fluid before quenching.

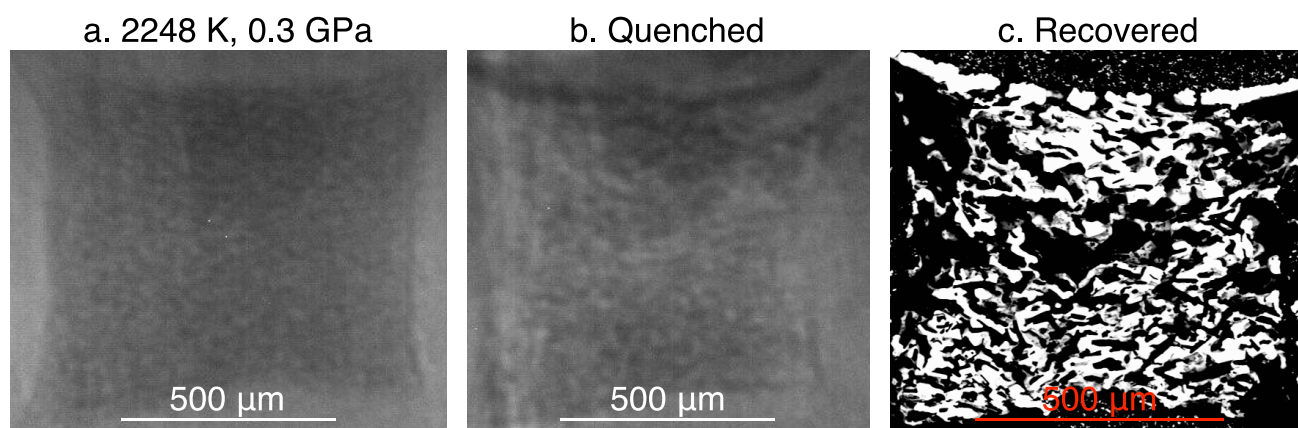


Figure S-5 X-ray radiographic and back-scattered-electron (BSE) images of the experiment run 5-18 quenched from 0.3 GPa and 2248 K with Fe-1.0 wt.% N-10.0 wt. % C as the starting composition. **(a, b)** *In-situ* X-ray radiographic images of the sample chamber at 0.3 GPa, 2248 K and after quenching in temperature. **(c)** BSE image of the recovered sample. Besides the void regions from N-rich supercritical fluid, graphite is also shown as black regions.

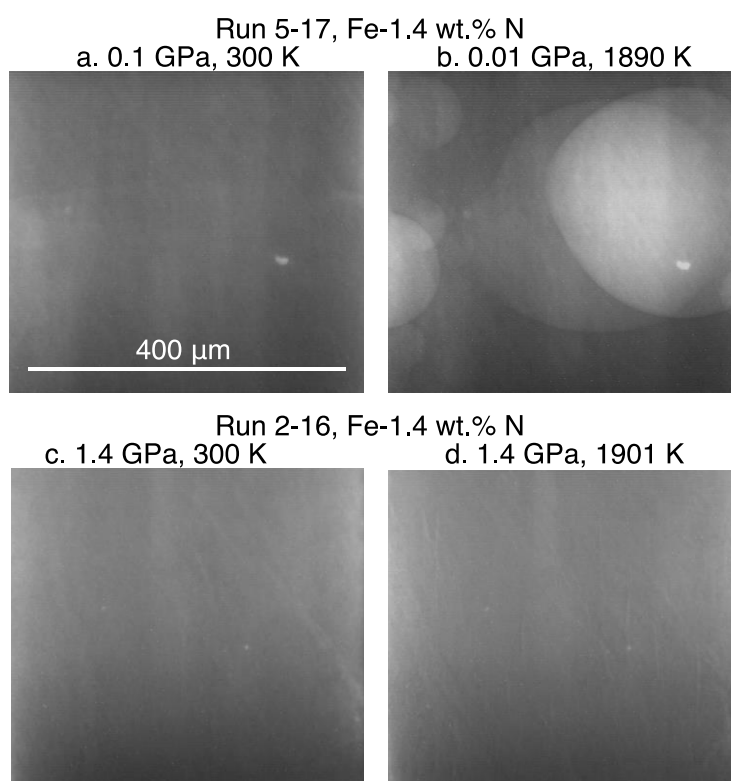


Figure S-6 The pressure dependence of the miscibility gap for Fe-1.4 wt. % N starting material observed via X-radiography. For experiment running near 1 bar (run 5-17, **a-b**), immiscible liquids persist to at least 1890 K. The miscibility gap in this composition is fully closed at 1.4 GPa (run 2-16, **c-d**).

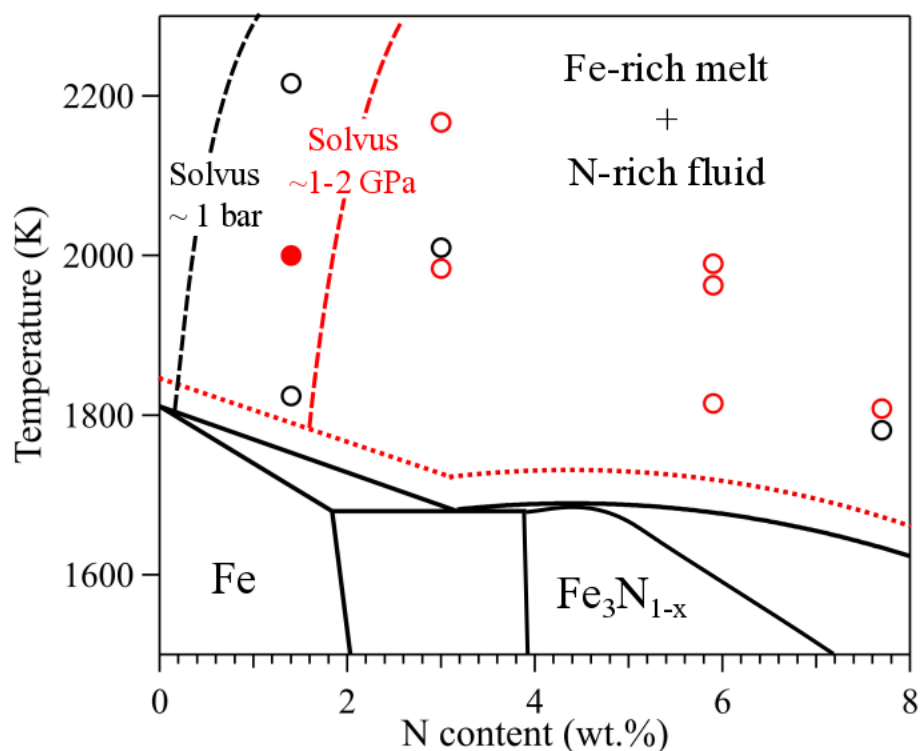


Figure S-7 The pressure-dependence of miscibility gap in Fe-N system. The black and red open circles show the relationships between quenching temperatures and initial N contents of experiments which show immiscible melting before quenching at ~ 1 bar and $\sim 1-2$ GPa, respectively. The red solid circle marks the experiment (Run 2-16) without showing immiscible melting at 1.4 GPa. The black and red dashed curves show the solvuses at ~ 1 bar and $\sim 1-2$ GPa, respectively, based on these experimental data. The black solid curves show the phase relations at 1 bar (Guillemet and Du, 1994) while the red dotted curve is extrapolated liquidus at 1 GPa anchored by Fe melting temperature (Anderson and Isaak, 2000).

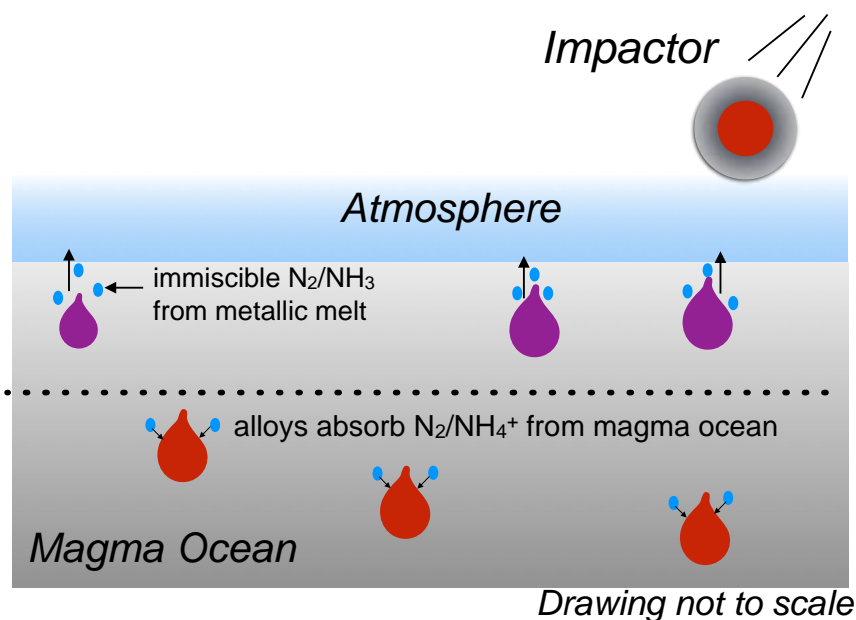


Figure S-8 Cartoon illustrating key processes that influence the BSE C/N ratio. In previous models of volatile behavior during accretion (*e.g.*, Bergin *et al.*, 2015; Hirschmann, 2016), C and N contents of the BSE are set by the amounts of volatiles lost (1) to the atmosphere or space during impact of planetesimals with the magma ocean and (2) to the core by metal-silicate partitioning and sinking of metallic droplets. These models are modified to include (3) effect of immiscible N-rich fluid and re-dissolution of N into the metallic phase at depths. The alloys from impactors are assumed to release N efficiently to space during collision with Earth's magma ocean and thus are N-depleted (purple droplets). The degassing N could be either N_2 or NH_3 , depending on fO_2 and pH conditions (Mikhail and Sverjensky, 2014). When such N-depleted metallic drops sink to deeper depths (illustrated by the dashed line), their N solubility increases and the interaction between such alloy with extremely high C/N ratio and magma ocean would increase the BSE C/N ratio during core formation.

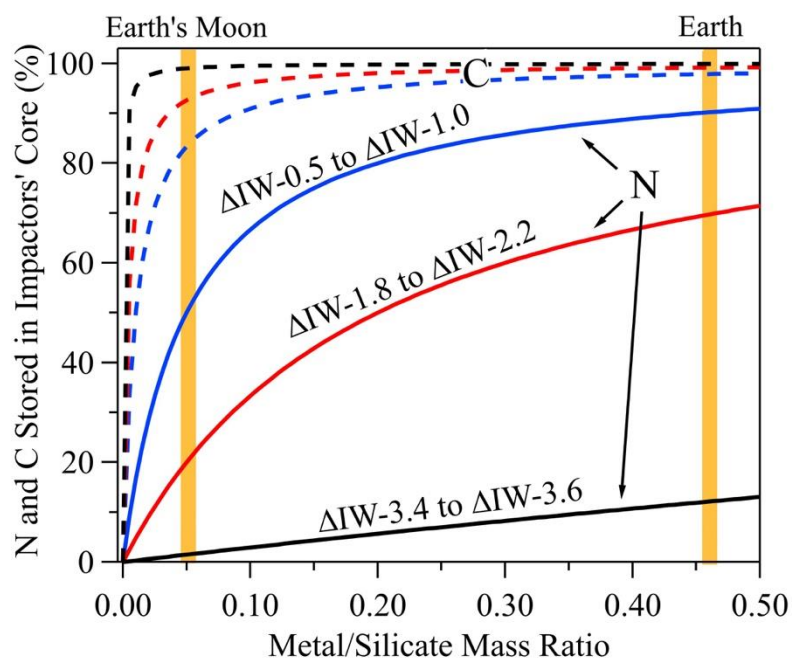


Figure S-9 The mass proportion of N and C stored in impactors' alloy phase, which would be lost to space via impacts. Assuming that the silicate and alloy of impactors fully equilibrated, N and C distribution is controlled by partition coefficients and mass ratio of the alloy and silicate phases. The solid curves are for N and the dashed curves are for C. The blue, red and black curves show the relationship between the proportion of N and C stored in the alloy phase of impactors and their metal to silicate mass ratio under slighted reduced ($\Delta IW-0.5$ to $\Delta IW-1.0$), reduced ($\Delta IW-1.8$ to $\Delta IW-2.2$) and very reduced ($\Delta IW-3.4$ to $\Delta IW-3.6$) conditions, respectively. The partition coefficients are from Dalou *et al.* (2017). The yellow vertical bars mark the core/mantle mass ratios for the Earth and its moon.

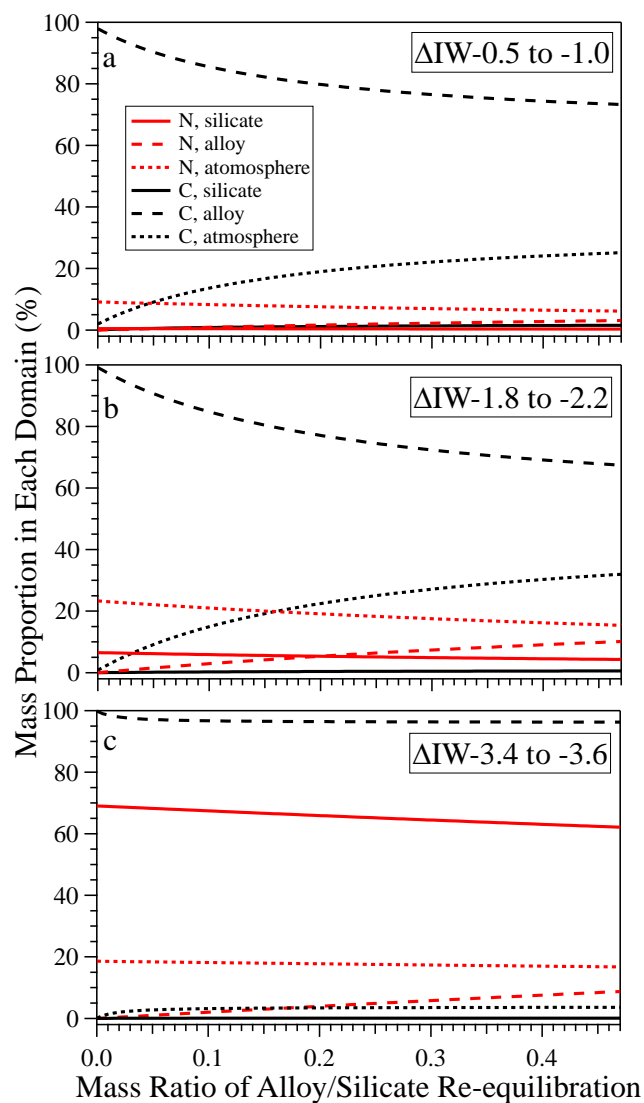


Figure S-10 After loss of immiscible N to space via impact, mass proportions of nitrogen (red) and carbon (black) distributed among the primordial atmosphere, magma ocean and core under different oxygen fugacity as a function of the degree of re-equilibration between alloy and silicate during core formation. The solid curves are for silicate mantle, the dashed curves are for the core and the dotted curves are for primordial atmosphere. From row one to three, oxygen fugacity is $\Delta IW-0.5$ to $\Delta IW-1.0$ (slightly reduced); $\Delta IW-1.8$ to $\Delta IW-2.2$ (reduced) and $\Delta IW-3.4$ to $\Delta IW-3.6$ (very reduced), respectively.



Supplementary Video

Supplementary Video S-1 can be downloaded at <http://www.geochemicalperspectivesletters.org/article1919>.

Video S-1 *In-situ* observation of Fe-N alloy (run 4-17) under high-pressure and high-temperature conditions by X-ray radiography. The upper-right corner shows *in-situ* temperature, oil pressure. The starting sample is Fe₃N at 0.4 GPa. Upon heating, immiscible melting occurs around 1726 K, as indicated by the presence of light bubbles. At higher temperatures, N-rich supercritical fluid partially dissolves into metallic liquid. Lowering temperatures re-exsolves N-rich supercritical fluid from metallic liquid. The camera frame rate is 3 frames/second.



Supplementary Information References

- Anderson, O.L., Isaak, D.G. (2000) Calculated melting curves for phases of iron. *American Mineralogist* 85, 376–385.
- Bergin, E.A., Blake, G.A., Ciesla, F., Hirschmann, M.M., Li, J. (2015) Tracing the ingredients for a habitable earth from interstellar space through planet formation. *Proceedings of the National Academy of Sciences* 112, 8965–8970.
- Dalou, C., Hirschmann, M.M., von der Handt, A., Mosenfelder, J., Armstrong, L.S. (2017) Nitrogen and carbon fractionation during core–mantle differentiation at shallow depth. *Earth and Planetary Science Letters* 458, 141–151.
- Dobson, D.P., Wiedenbeck, M. (2002) Fe- and C-self-diffusion in liquid Fe₃C to 15 GPa. *Geophysical Research Letters* 29, 2-1-2–4.
- Grewal, D.S., Dasgupta, R., Sun, C., Tsuno, K., Costin, G. (2019) Delivery of carbon, nitrogen, and sulfur to the silicate Earth by a giant impact. *Science Advances* 5, eaau3669.
- Hirschmann, M.M. (2016) Constraints on the early delivery and fractionation of Earth's major volatiles from C/H, C/N, and C/S ratios. *American Mineralogist* 101, 540–553.
- Kono, Y., Irifune, T., Higo, Y., Inoue, T., Barnhoorn, A. (2010) P-V-T relation of MgO derived by simultaneous elastic wave velocity and in situ X-ray measurements: A new pressure scale for the mantle transition region. *Physics of the Earth and Planetary Interiors* 183, 196–211.
- Kono, Y., Kenney-Benson, C., Shibasaki, Y., Park, C., Wang, Y., Shen, G. (2015) X-ray imaging for studying behavior of liquids at high pressures and high temperatures using Paris-Edinburgh press. *Review of Scientific Instruments* 86, 072207.
- Kono, Y., Park, C., Kenney-Benson, C., Shen, G., Wang, Y. (2014) Toward comprehensive studies of liquids at high pressures and high temperatures: Combined structure, elastic wave velocity, and viscosity measurements in the Paris–Edinburgh cell. *Physics of the Earth and Planetary Interiors* 228, 269–280.
- Mikhail, S., Sverjensky, D.A. (2014) Nitrogen speciation in upper mantle fluids and the origin of Earth's nitrogen-rich atmosphere. *Nature Geoscience* 7, ngeo2271.

